Isotropy and the Kármán-Howarth-Kolmogorov relation in experimental and numerical turbulence

Masanori Takaoka*
Department of Mechanical Engineering, Doshisha University, Kyotanabe, Kyoto 610-0321, Japan

Hideaki Mouri,† Akihiro Hori, and Yoshihide Kawashima
Meteorological Research Institute, Nagamine, Tsukuba 305-0052, Japan

(Received 25 September 2006; revised manuscript received 19 September 2007; published 19 December 2007)

The evolutions of isotropy and the Kármán-Howarth-Kolmogorov (KHK) relation are studied experimentally and numerically in the lifetime of turbulence, i.e., developing, fully developed, and decaying states. The isotropy relations and the KHK relation are well satisfied when the turbulence is fully developed, but they are broken when the turbulence is developing or decaying. The turbulence shows opposite anisotropy in the developing and the decaying states. In response to the isotropy change, the KHK relation shows a variation of energy budget at each scale, which is consistent with an energy transfer from large to small scales. We also find that Taylor's frozen-eddy hypothesis and periodic boundary conditions, respectively, lead to an inherent phenomenon at large scales.

DOI: 10.1103/PhysRevE.76.066312 PACS number(s): 47.27.Ak, 47.27.Gs

I. INTRODUCTION

Assuming isotropy and homogeneity, von Kármán and Howarth [1] first established the Kármán-Howarth (KH) relation directly from the Navier-Stokes equation. It has played a fundamental role in all subsequent turbulence studies. Kolmogorov [2] rewrote the KH relation in the form connecting a second-order longitudinal structure function $D_{LL}(r,t)=\langle(\delta u_L)^2\rangle$ to a third-order longitudinal structure function $D_{LLL}(r,t)=\langle(\delta u_L)^3\rangle$,

$$-D_{LLL}(r,t)+6\nu\frac{\partial D_{LL}}{\partial r}(r,t)=\frac{4}{5}\epsilon r, \tag{1}$$

with the implicit assumption of steady state. Here $\delta u_L(r,t)$ is the longitudinal velocity increment of u_L over the separation r, and ϵ and ν are the mean energy dissipation rate and the kinematic viscosity, respectively. The modified form of the relation for decaying turbulence,

$$-\frac{3}{r^4}\int_0^r\frac{\partial D_{LL}}{\partial t}s^4ds-D_{LLL}(r,t)+6\nu\frac{\partial D_{LL}}{\partial r}(r,t)=\frac{4}{5}\epsilon r, \tag{2}$$

was given in Refs. [3,4]. We here call it the Kármán-Howarth-Kolmogorov (KHK) relation.

In the so-called inertial range at sufficiently high Reynolds numbers, Kolmogorov derived the statistical law for the third-order structure function

$$-D_{LLL}(r)=\frac{4}{5}\epsilon r, \tag{3}$$

which is called Kolmogorov's 4/5 law [2]. Although the 4/5 law requires r to be in the inertial range, the KHK relation holds for arbitrary r and Reynolds number in so far as the flow is homogeneous and isotropic.

Most work on the verification of these relations has been done for small scales in a fully developed state, because Kolmogorov's theory [5,6] predicts universally isotropic behavior there. Turbulence at large scales usually loses isotropy and homogeneity due to the energy-containing mechanism. Freely decaying turbulence may show changes of its isotropy even at large scales by the nonlinear interaction among scales. However, little is known about the isotropizing or anisotropizing process at each scale in the evolution of turbulence.

Turbulence experiences three states in its lifetime, i.e., developing, fully developed, and decaying states. In our previous work [7,8], we found that the probability density function (PDF) of velocity fluctuations changes accordingly from sub-Gaussian to Gaussian and to super-Gaussian. In Ref. [9], we showed that even in large-scale behavior there exists a universal statistical property.

We here focus our attention on the changes of isotropy and the KHK relation at large scales in these three states. As far as we know, no one has reported how these relations are broken in developing and decaying states until now.

Laboratory experiments and numerical simulations play mutually complementary roles. In experiments, one can reach high Reynolds numbers but their measurement is restricted to one or two dimensions. Taylor's frozen-eddy hypothesis [10] identifies a velocity signal $u(t)$ measured by a fixed probe with $u(-x/U)$ if the mean velocity U is large enough. In other words, this hypothesis converts the laboratory frame (x_L,t_L) into a virtual frame, the so-called Taylor frame, (x_T,t_T) by $x_T=-Ut_L$ and $t_T=x_L/U$ [9,11]. The mean energy dissipation rate ϵ, which is an essential quantity in turbulence analysis, is notoriously difficult to measure. It is in fact reported that the results for the KHK relation are strongly dependent on the estimates of ϵ [12,13]. On the other hand, in numerical simulations, all physical quantities including ϵ can be calculated, although large-scale quantities

*mtakaoka@mail.doshisha.ac.jp
†hmouri@mri-jma.gp.jp

always suffer from somewhat artificial boundary conditions and forcing. It is notoriously difficult to analyze inertial range properties, not to speak of large-scale motion far beyond an integral length. To exclude artifacts in numerical simulations, it is important to compare the results with those of experiments and/or to extract common features from simulations of different conditions.

In this paper, we study grid turbulence experimentally and periodic-box turbulence numerically. Since both turbulences show excellent isotropy in the fully developed state, we have the advantage that there is no need to extract isotropic components such as those proposed in Refs. [14–17]. In the following section, the experimental setup and the numerical procedure are explained and the relevant data are summarized. Concentrating on large-scale behaviors, we discuss the evolution of the isotropy of turbulence in Sec. III, and that of the KHK relation in Sec. IV. The last section is devoted to a summary and discussion.

II. EXPERIMENTAL SETUP AND NUMERICAL PROCEDURE

A. Grid turbulence

The experiment was done in a wind tunnel at the Meteorological Research Institute. Its size was, respectively, 18, 3, and 2 m in the streamwise, spanwise, and floor-normal directions. The grid consisted of two layers of uniformly spaced rods, the axes of which were perpendicular to each other. The separation of the axes of adjacent rods was 0.40 m, and the cross section of the rods was 0.06×0.06 m^2. The mean wind velocity U was set to be $U \approx 11$ m s^{-1}. Note that grid turbulence is spatially evolving turbulence, where the disturbance produced by grid evolves into a more complex field by mutual interaction while being swept downstream. It thus allows us to study developing, fully developed, and decaying states by changing the distance of the probe from the grid [7,8,18,19].

We then simultaneously measured the streamwise, $U+u$, and transverse, v, velocities by using a hot-wire anemometer. The measurements were done on the tunnel axis from $d=3.0$ to 16.0 m, where d is the distance from the grid. The hot-wire anemometer was composed of a crossed-wire probe and a constant-temperature system. The wires were 5 μm in diameter, 1.25 mm in effective length, 1.0 mm in separation and oriented at ±45° to the streamwise direction. The wire temperature was kept at 280 °C, while the air temperature was 12–13 °C. We calibrated the anemometer before and after the measurements. The signal was low-pass filtered with 24 dB/octave and sampled digitally with 16-bit resolution. The filtering was at 15 kHz and sampling was at 30 kHz. The entire length of signal data was as long as 1×10^7 points. Three sets of signal data were obtained at each distance.

In Table I, we summarize the flow parameters of our grid turbulence at each distance. The mean velocity U gradually decreases as the distance d increases. The Taylor microscale Reynolds number Re_λ decreases at $d \lesssim 5.0$ m, and becomes almost constant in the range $5.0 \lesssim d \lesssim 14.0$ m, and then gradually increases at $d \gtrsim 12.0$ m. We here use $\mathrm{Re}_\lambda = \langle v^2 \rangle^{1/2} \lambda / \nu$, where $\lambda = [2\langle v^2 \rangle / \langle (\partial_x v)^2 \rangle]^{1/2}$ is the Taylor microscale [20]. The transverse integral length $L_v = \int \langle v(x) v(x+r) \rangle / \langle v(x)^2 \rangle dr$ gradually increases with d [21]. At $d \gtrsim 14.0$ m, L_v is about 0.072 m after a steplike increment. The large-scale flow then seems to have different characteristics from those at $d \lesssim 13.0$ m.

TABLE I. Summary of flow parameters at each distance d. They are written in SI units. The bold numbers in the first column are the representative distances used in later analysis.

d	U	L_v	$\langle u^2 \rangle^{1/2}$	$\langle v^2 \rangle^{1/2}$	ϵ_u	ϵ_v	Re_λ
3.0	11.4	0.033	1.00	0.94	7.0	6.3	357
3.5	11.2	0.035	0.87	0.82	4.7	4.3	334
4.0	11.1	0.035	0.77	0.73	3.2	3.1	315
4.5	11.1	0.040	0.70	0.66	2.4	2.3	300
5.0	11.0	0.042	0.61	0.59	1.8	1.8	264
6.0	10.9	0.045	0.54	0.53	1.1	1.1	265
7.0	10.9	0.049	0.49	0.47	0.71	0.71	266
8.0	10.8	0.051	0.44	0.43	0.51	0.50	263
9.0	10.8	0.057	0.40	0.39	0.39	0.38	258
10.0	10.8	0.062	0.38	0.37	0.31	0.30	257
11.0	10.7	0.062	0.36	0.35	0.26	0.24	259
12.0	10.7	0.061	0.34	0.34	0.22	0.21	260
13.0	10.6	0.063	0.33	0.33	0.20	0.18	263
14.0	10.6	0.073	0.33	0.33	0.18	0.17	266
15.0	10.6	0.072	0.32	0.32	0.17	0.15	275
16.0	10.6	0.072	0.32	0.33	0.16	0.14	284

Isotropy at each scale can be estimated by the directional dependence of the flow parameters in Table I. The flow becomes isotropic at $d \gtrsim 6.0$ m for the velocity fluctuations $\langle u^2 \rangle^{1/2}$ and $\langle v^2 \rangle^{1/2}$, and at $d \gtrsim 4.0$ m for the energy dissipations $\epsilon_u = 15\nu \langle (\partial_x u)^2 \rangle$ and $\epsilon_v = 15\nu \langle (\partial_x v)^2 \rangle / 2$ [10]. We notice that the small-scale isotropy precedes the large-scale isotropy.

In the following analysis, we choose the distances $d=4.0$, 10.0, and 15.0 m as representative of the developing, fully developed, and decaying states respectively.

The ratios of the magnitude of the velocity fluctuations u and v to the mean streamwise velocity U were always smaller than 0.2. This small ratio allows us to rely on Taylor's frozen-eddy hypothesis. It should be noted here that, since the time of the entire data set was 333 s, the entire length of the converted space is approximately 3.7 km, which is much larger than our experimental apparatus. In order to emphasize this fact, we here call the converted frame the Taylor frame [9].

B. Numerical turbulence

We also performed direct numerical simulations of decaying turbulence using the computer code in Ref. [22]. The governing equations for an incompressible fluid are the vorticity equation

$$\partial_t \boldsymbol{\omega} = \boldsymbol{\nabla} \times (\boldsymbol{u} \times \boldsymbol{\omega}) + \nu \nabla^2 \boldsymbol{\omega} \tag{4}$$

and the continuity equation

$$\nabla \cdot \boldsymbol{u} = 0, \tag{5}$$

where $\boldsymbol{\omega}=\nabla\times\boldsymbol{u}$ is the vorticity. No forcing is added. The method used in the simulation was a standard pseudospectral method to calculate the nonlinear terms under the assumption of a periodic boundary condition. The aliasing errors were removed by a phase-shifted polyhedral truncation. The time marching was performed by the fourth-order Runge-Kutta-Gill method with exact integration of the linear terms.

In order to simulate grid turbulence, the initial field was set to be composed of organized vortices and an isotropic Gaussian random field. The former was given by a vortex array that consists of alternately rotating vortices: $\boldsymbol{\omega}(x,y,z)=(A\sin(k_y y)\sin(k_z z),0,0)$, where A, k_y, and k_z were constants. Behind a grid in the wind tunnel, each jet induces formation of a series of vortex rings, which is shown as a peak in the energy spectra of Fig. 5(a) in Ref. [7]. A two-dimensional array of intensified vortices, called a "rib," is formed by streamwise elongation between the vortex rings. On the other hand, the isotropic Gaussian random field was given the form of the energy spectrum

$$E(k,0) = Ck^4 \exp\left(-\frac{k^2}{k_0^2}\right), \tag{6}$$

where k_0 and C are constants and k is the norm of the wave numbers [23,24]. We here report the results for the parameter values $(A,k_x,k_y,C,k_0)=(10\sqrt{2},2,2,1.17\times10^{-1},2)$, which were chosen so that both the initial enstrophy density $\Omega=\langle\omega^2\rangle/2$ of the vortex array and that of the Gaussian random field are 25. Since the characteristic length scales of the two fields, (k_x^{-1},k_y^{-1}) and k_0^{-1}, were the same, both the fields had almost the same energy.

In the following sections, the results for the simulations with grid points $N^3=512^3$ are reported. The maximum wave number is given by $k_{\max}=\sqrt{3}N/2$. The reliability of the spatial resolution of our simulation is estimated by $k_{\max}\eta$, where $\eta=(\nu/\epsilon)^{1/4}$ is the Kolmogorov length. In our numerical simulation, the value was always larger than 1.66. The following figures for the simulations were obtained by averaging over 20 realizations with different random fields.

In Figs. 1 and 2, the time dependences of Re_λ and $\epsilon=2\nu\Omega$ are summarized, respectively. Re_λ decreases rapidly until $t\approx1.5$, and then becomes almost constant. It should be noted that Re_λ decreases from the start, which is the case for turbulence starting from a large-scale flow with no forcing [25,26]. Since the energy density E decreases gradually and ϵ increases rapidly, then $\mathrm{Re}_\lambda=2\sqrt{5E}/\sqrt{3\nu\epsilon}$ decreases rapidly in the early period.

Large-scale vortices are stretched to have thin sheet structures up to the enstrophy-maximum time, and then viscosity induces instability to make sheet vortices into tube vortices [22,27,28]. We here define the developing state as a state when small-scale structures are created and grow. In such a state, the energy spectrum spreads to a higher-wave-number range. The transition time to the fully developed state is estimated by the enstrophy-maximum time $t\approx1$.

Independence of ϵ from ν is postulated in Kolmogorov's first similarity hypothesis [5]. In order to see this independence, we also have done simulations with $N=256$, whose Re_λ and ϵ are shown by the dashed lines in Figs. 1 and 2, respectively. Figure 2 shows that ϵ is almost independent of ν in $2\lesssim t\lesssim4$, where we define the field as a fully developed state. For the rest of the lifetime, defined as a decaying state, Re_λ decays almost exponentially as shown in Fig. 1. At the final time, ϵ is almost 1/1000 part of its maximum value, while Re_λ is still larger than half of the values in the developed state.

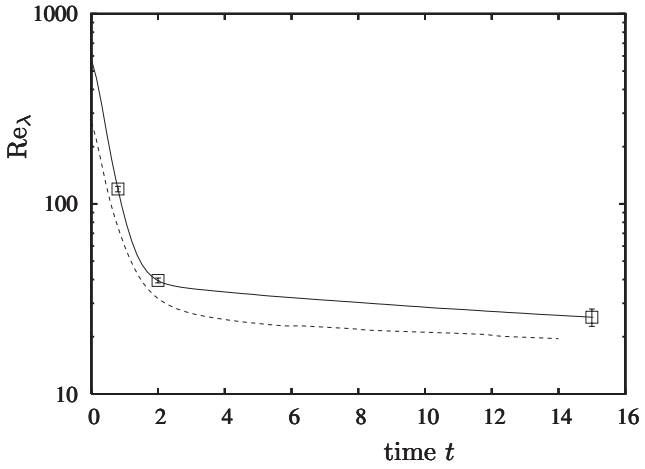

FIG. 1. Time dependence of Re_λ. The solid and dashed lines represent the results for $N=512$ and 256, respectively. The square symbols are the representative times used in later analysis.

We choose three times $t=0.8$, 2.0, and 15 as representative of the developing, fully developed, and decaying states, respectively. They are shown by the square symbols in Figs. 1 and 2 with the error bars representing the statistical variance.

The assumption of a periodic boundary condition with finite length restricts us to considering discrete Fourier series with given lowest wave number. In order to emphasize this fact, we here call the simulated frame the discrete Fourier frame.

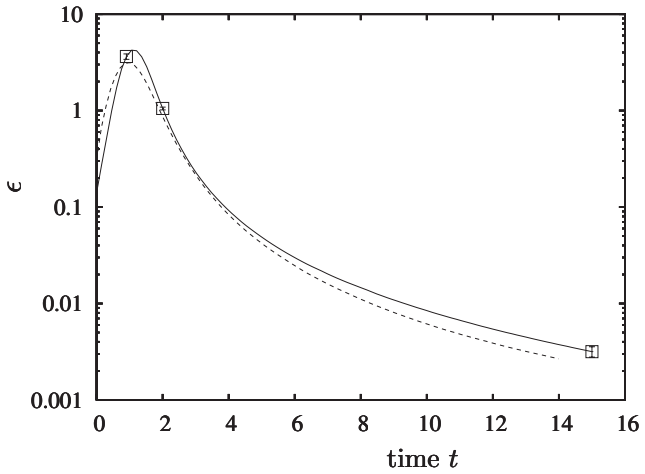

FIG. 2. Time dependence of ϵ. See also the caption of Fig. 1.

III. ISOTROPY RELATION

Isotropy as well as homogeneity are indispensable for the KHK relation. By comparing statistical quantities such as those in Table I [10,18,19], one can make only a crude estimation of isotropy. In order to examine the isotropy at each scale, we use the isotropy relations for the second- and third-order structure functions for an incompressible fluid [1,5,29],

$$D_{LL}(r,t) + \frac{r}{2}\frac{\partial D_{LL}}{\partial r}(r,t) = D_{TT}(r,t), \tag{7}$$

$$\frac{1}{6}\frac{\partial r D_{LLL}}{\partial r}(r,t) = D_{LTT}(r,t), \tag{8}$$

where $D_{TT}=\langle(\delta u_T)^2\rangle$, $D_{LTT}=\langle \delta u_L(\delta u_T)^2\rangle$, and δu_T is the transverse velocity increment over the separation r. It is preferable to integrate these relations once with respect to r to reduce numerical errors in calculating derivatives in Eqs. (7) and (8) [30]:

$$D_{LL}(r,t) = \frac{2}{r}\int_0^r \left(D_{TT}(s,t) - \frac{1}{2}D_{LL}(s,t)\right)ds, \tag{9}$$

$$-D_{LLL}(r,t) = -\frac{6}{r}\int_0^r D_{LTT}(s,t)ds. \tag{10}$$

Note that the left-hand side (LHS) of these equations is still local in r. We examine these relations in this section.

A. Isotropy relations in the Taylor frame

We first check the isotropy relations for the experimental data. It must be noted that in this section we use the notation in the Taylor frame.

Figures 3(a)–3(c) show the graphs of the RHS and LHS of Eqs. (9) and (10) at the representative distances. The second- and third-order structure functions are drawn, respectively, by the upper two lines and the lower two lines. The horizontal axis represents the separation r in units of the Kolmogorov length η.

From the upper two lines, we see that the relation (9) is almost satisfied in the entire range of r and becomes better with increasing distance d from the grid in the large-scale region $r/\eta \gtrsim 10^2$. It should be emphasized that the isotropy relation approximately holds beyond the size of the wind tunnel, not to mention the integral length $L \approx 2L_v$ shown by the arrow in each figure.

For the third-order structure function, the RHS of Eq. (10) is larger than the LHS at scales smaller than the integral lengths. At the larger scales, the relative amplitude of the RHS to the LHS becomes lower as d increases [see the changes in Figs. 3(a)–3(c)]. The negative values of the RHS in the range $10^2 \lesssim r/\eta \lesssim 10^4$ develop to form a large peak of plus symbols. These large-scale behaviors indicate that energy transfer from the large scale decreases and large-scale vortical motions are enhanced.

Constancy at scales larger than the integral length is equivalent to the fact that the velocity correlation vanishes above the integral length. In theory, the second-order structure functions converge to twice the variance of each velocity component, while the third-order ones converge to zero. The scattering of the third-order ones on a much larger scale shows the level of statistical fluctuation in our experimental data.

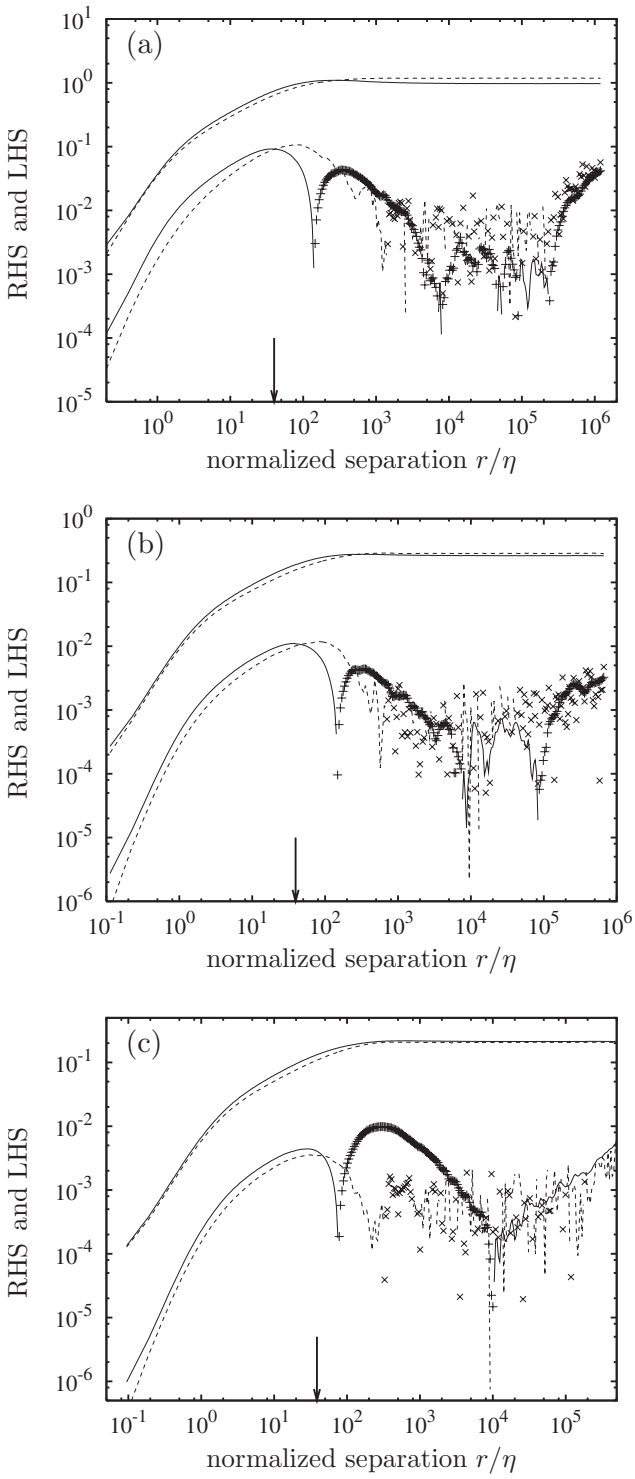

FIG. 3. Isotropy relations at (a) 4, (b) 10, and (c) 15 m. The solid and dashed lines represent the RHS and LHS, respectively. The plus and cross symbols denote the negative values of the RHS and LHS. The arrow shows the integral length.

Information about the isotropy known from Table I is included in the graphs of the second-order structure functions. The isotropy relation between $\langle u^2\rangle^{1/2}$ and $\langle v^2\rangle^{1/2}$ is shown in the graphs at large scales as mentioned above. The isotropy relation between ϵ_u and ϵ_v is also shown in the graphs at the smallest scales. But the anisotropy observed in the third-order structure functions is not reflected in the quantities listed in Table I, because they essentially consist of second-order moments. For the KHK relation, however, the third-order structure functions are significant in the inertial range, and may affect this relation.

B. Isotropy relations in the discrete Fourier frame

It is generally hard to investigate large-scale behavior in a numerical simulation of turbulence. As we saw in the previous section, however, the large-scale behavior of the isotropy relation can be extrapolated from the behavior around the integral length, so that we can examine large-scale statistics, if the simulated box is considerably larger than the integral scale.

The isotropy relations at the three representative times are shown in Figs. 4(a)–4(c). Although the initial organized vortices had unidirectional anisotropy, the following figures were obtained by averaging over the three directions of the periodic box. Crude isotropy is then satisfied, and the breaking of the isotropy relations is due to the Navier-Stokes dynamics. Error bars are drawn every 25 data points to avoid being dense at large scales. The integral length $L=3\pi\int E(k)k^{-1}dk/4\int E(k)dk\approx L_u\approx 2L_v$ is shown by the arrow in each graph [31]. It should be noted that the correlation length is usually comparable with the periodic length in the discrete Fourier frame.

For the second-order structure function, the isotropy relation holds at all scales. Taking a closer look at the upper two lines at scales larger than the integral length, one can recognize that they show the same tendency as observed in Fig. 3. The difference between the two lines at each time is very small, but statistically significant even allowing for the statistical error. The dashed line is above the solid line in the developing state. Both the lines are overlapping in the fully developed state. The dashed line is below the solid line in the decaying state.

The RHS and LHS of Eq. (10), the lower two lines, depart from each other around the integral length. In the developing state, the LHS is larger than the RHS at large scales. In the fully developed state, the relation (10) holds within the margin of error in the whole range. In the decaying state, the RHS is larger than the LHS at large scales, which is a reversal of the positional relation from the developing state. These results are consistent with the experimental results except for the large peak of plus symbols observed in Fig. 3(c). The strong decline at the right end of the dashed line in Fig. 4(c) indicates that one may observe this large peak of plus symbols if a discrete Fourier frame with much larger periodic length is used.

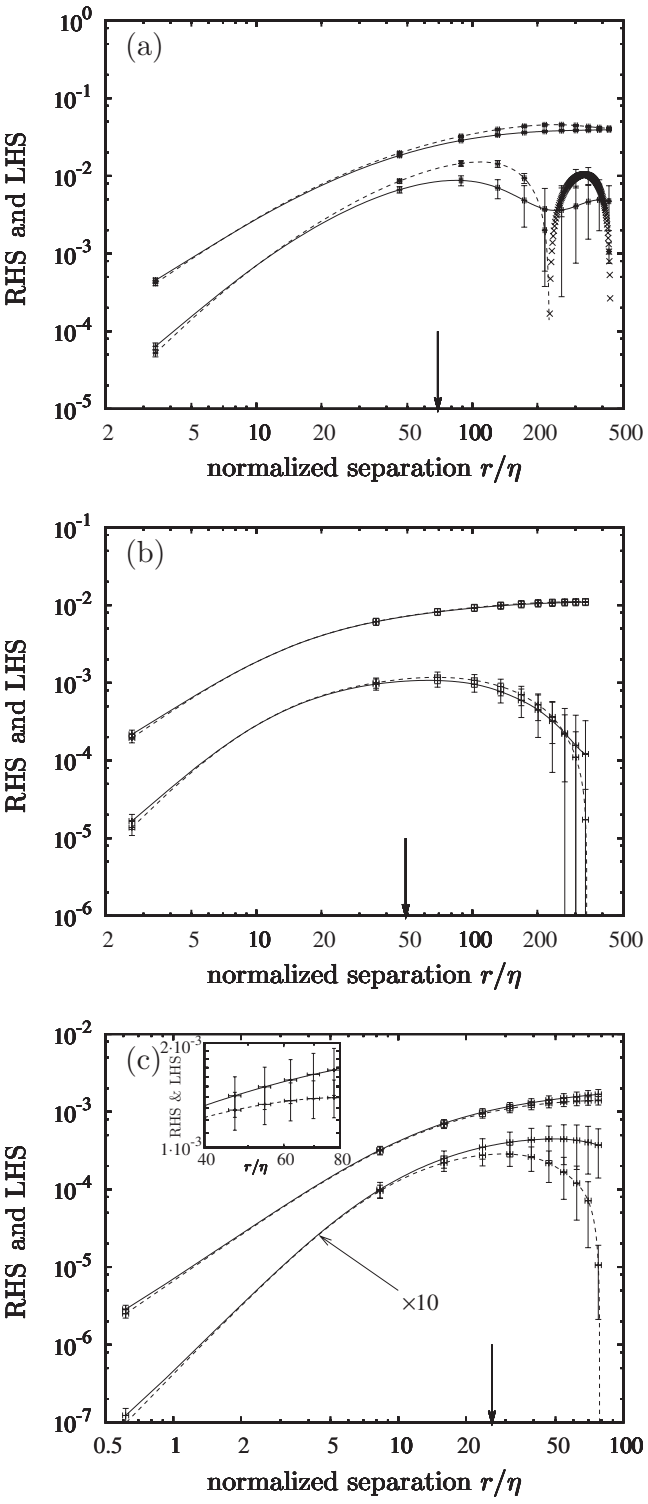

FIG. 4. Isotropy relations at t=(a) 0.8, (b) 2.0, and (c) 15. See also the caption of Fig. 3. The error bars are drawn every 25 data points. The lower two lines in (c) are multiplied by 10 for graphical convenience. Inset: Enlargement of the rightmost region for the upper two lines.

IV. KÁRMÁN-HOWARTH-KOLMOGOROV RELATION

The flow fields show a different nature of anisotropy in each state as described above. In this section, let us consider how such anisotropy appears in the KHK relation. The KHK relation for decaying homogeneous isotropic turbulence is written as Eq. (2). A scale-by-scale energy budget is obtained from the KHK relation. Each term on the LHS in the order

from left to right expresses the unsteadiness, the energy transfer, and the viscous dissipation, which are hereinafter referred to as the unsteadiness, the transfer, and the dissipation terms, respectively.

A. KHK relation in the Taylor frame

Figures 5(a)–5(c) show each term in the LHS of Eq. (2), which is normalized by the RHS at each representative distance. The unsteadiness term stems from the inhomogeneity in the laboratory frame. This term was estimated from adjacent-distance data, i.e., data at 3.5 and 4.5 m for 4 m, data at 9 and 11 m for 10 m, and data at 14 and 16 m for 15 m [9,11]. The solid line in each figure represents the sum of the quantities in the LHS normalized by the RHS, so that its value is unity when the KHK relation is satisfied. We here estimate ϵ by ϵ_v [20].

The constant value at large scales is different in the three states. When the turbulence is developing, the value is slightly larger than unity. When the turbulence is fully developed, it is close to unity. The KHK relation holds in the whole range, though the 4/5 law is not attained. When the turbulence is decaying, the value is smaller than unity. The turbulence intensity has become weak; therefore the graph is a little rough.

The KHK relation is exactly derived under the assumption of isotropy and homogeneity. In the present turbulence, the homogeneity in the Taylor frame is well satisfied. Figures 3(b) and 5(b) show that the isotropy relations hold when the field is fully developed. The discrepancies from unity at large scales in Figs. 5(a) and 5(c) correspond to the different nature of anisotropy discussed in Sec. III A.

The constancy at large scales is explained as follows. The transfer and the dissipation terms become negligible at large scales. If r is much larger than the integral length, then $D_{LL}(r,t) \approx 2\langle u^2 \rangle(t)$, so that the LHS as well as $\partial D_{LL}(r,t)/\partial t$ is constant with respect to r at each time t. This holds independently of the isotropy.

B. KHK relation in the discrete Fourier frame

Figures 6(a)–6(c) show the normalized quantities in the LHS of Eq. (2). We use the expression $\epsilon = 2\nu\Omega$, which is exact under periodic boundary conditions.

In the developing state, the sum of the normalized quantities in the LHS is larger than unity in the range where the unsteadiness term or the transfer term is large. This means an excess of energy transfer at large scales over the energy dissipation. The hump of the solid line in Fig. 6(a) is distributed on scales almost half of the characteristic length of the initially given vortex array, which corresponds to the breakup of eddies. The unsteadiness term is localized over scales larger than the integral length, stemming from the large-scale initial condition of Eq. (6). The dotted line is located above the solid line at the largest scales where the transfer term is negative. This means a redistribution of energy according to the isotropization of the large-scale flow. The transfer term exceeds the RHS in the range $20 \lesssim r/\eta \lesssim 70$ where the unsteadiness term is negative. The energy spectrum in this range is rapidly increasing, since much larger energy than the dissipation is supplied from the large scales. The dissipation extends to $r \approx 30\eta$ because of the undeveloped inertial range.

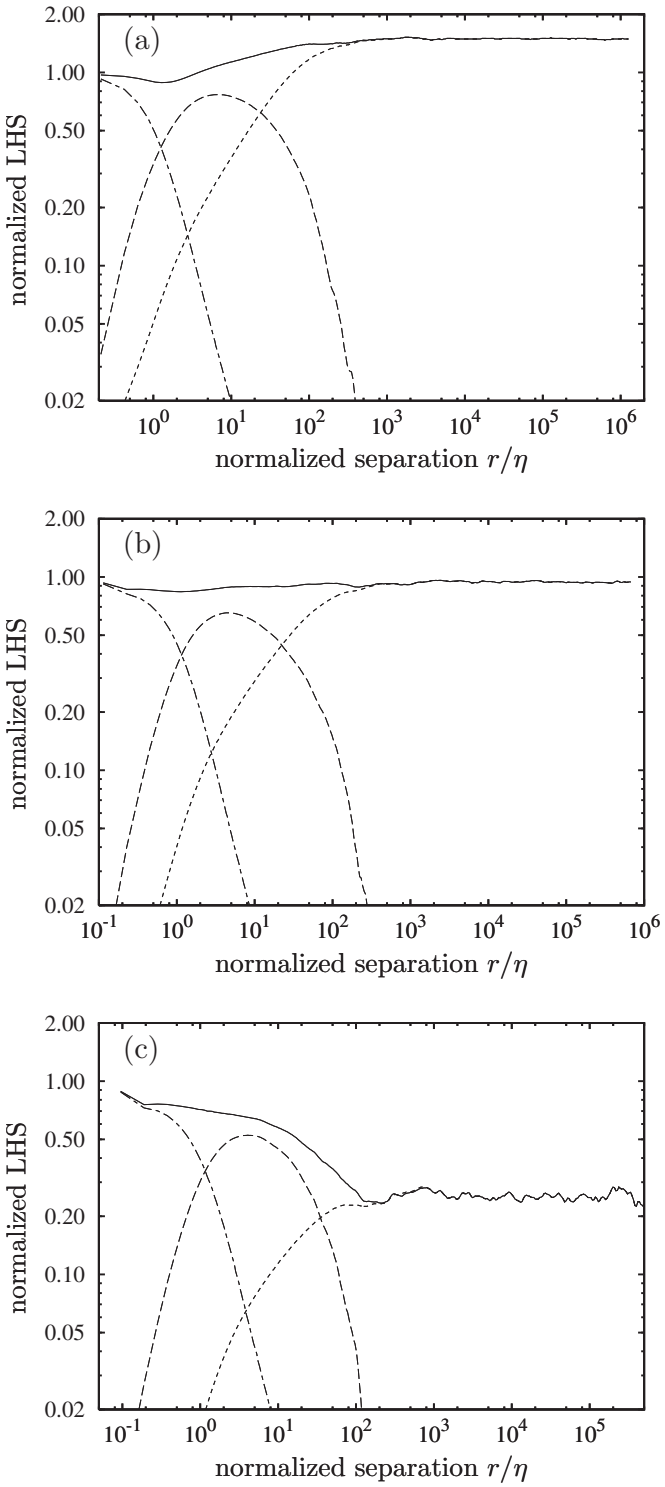

FIG. 5. KHK relation at (a) 4, (b) 10, and (c) 15 m. The dotted, dashed, and dot-dashed lines represent, respectively, the unsteadiness, the transfer, and the dissipation terms.

As the turbulence develops, the unsteadiness term extends to smaller scales, while the dissipation term shrinks from large scales. The transfer term decays and shifts to smaller scales. In the fully developed state, though no power-law

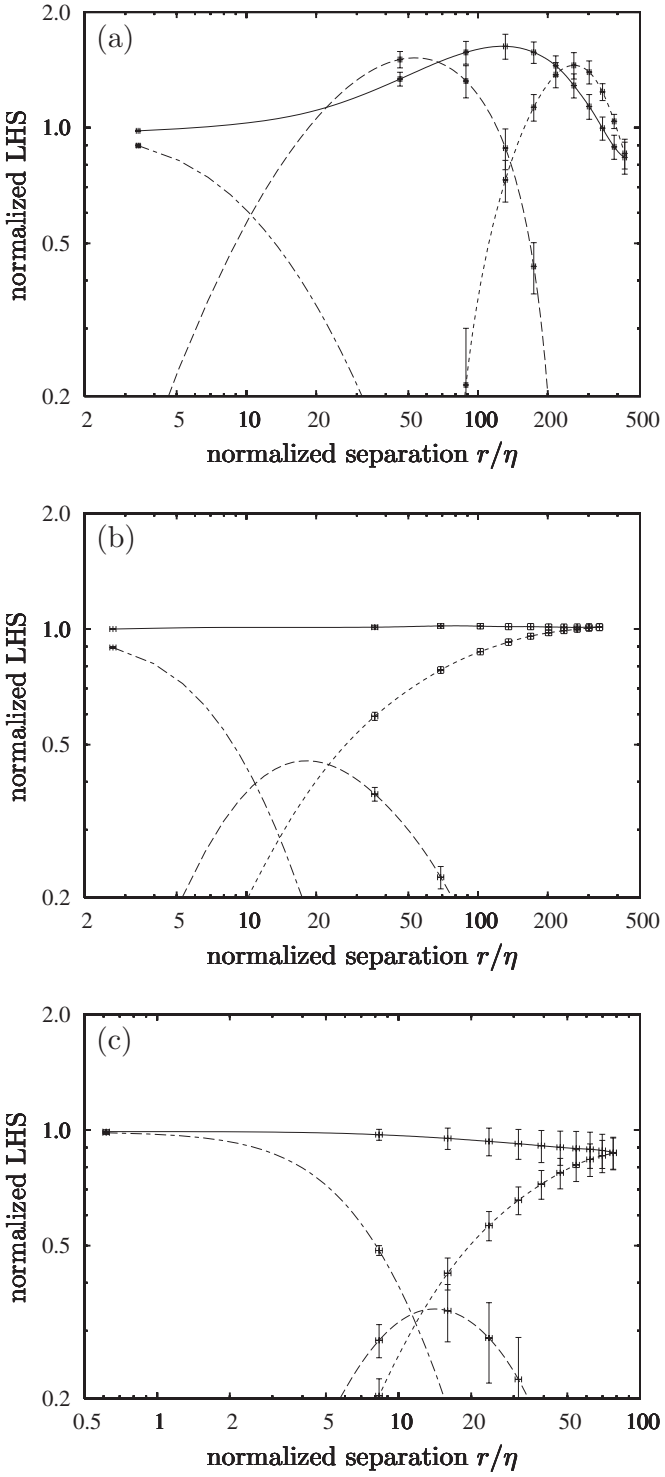

FIG. 6. KHK relation at t=(a) 0.8, (b) 2.0, and (c) 15. See also the caption of Fig. 5. The error bars are drawn every 25 data points to avoid being dense at large scales.

region is observed in Fig. 4(b), the KHK relation is perfectly satisfied at all scales [see the solid line in Fig. 6(b)].

In the decaying state, the dissipation term becomes dominant and the unsteadiness term decays as a whole. The transfer term decays and shifts to larger scales. These facts indicate that the energy supply from large scales falls below the dissipation at small scales. The solid line is downward sloping and below the value 0.9 at the largest scales. Although the statistical fluctuation becomes large at large scales in the decaying state, we can safely say that the solid line tends to be smaller than unity. These results are consistent with those observed in the Taylor frame, and this tendency is also confirmed in the simulations starting from other initial conditions. These facts lead us to expect that such behavior is universal.

V. SUMMARY AND DISCUSSION

We have examined the isotropy and the KHK relations in the Taylor and the discrete Fourier frames. We have clarified how the KHK relation as well as the isotropy relations are broken in the developing or decaying states. The intrinsic properties of turbulence should be separated from the properties inherent in each frame. In the Taylor frame, the second-order structure functions satisfy the isotropy relation even at extraordinarily large scales, more than 1 km, as shown in Sec. III A. In the discrete Fourier frame, the normalized unsteadiness term does not always show a constant value even at the largest scales, as shown in Sec. IV B. But there exist commonly observed behaviors, which are considered intrinsic and summarized in the following.

When the turbulence is developing, the unsteadiness and the transfer terms are larger than the values expected from the KHK relation. The turbulent kinetic energy is localized at large scales, which breaks the isotropy of the flow. Since vortex stretching enhances energy transfer, it is natural that the longitudinal structure functions are larger than the values expected from the isotropy relations. As the turbulence develops, the successively generated vortices of various sizes begin to interact. These active interactions cause the excess transfer of energy until sufficiently small vortices for dissipation are generated.

When the turbulence is fully developed, our simulation shows good isotropy for the third-order structure functions as well as the second-order ones in the whole range, though they were started from initial conditions with a unidirectionally anisotropic vortex array. The energy is transferred from large to small scales in a uniformly distributed manner. The KHK relation is well satisfied at all scales, including much larger scales than the integral length, as mentioned for the isotropy relations in the experimental data.

When the turbulence is decaying, the unsteadiness term is smaller than the value expected from the KHK relation. The energy left at large scales is not sufficient to supply the transfer compensating the dissipation at small scales, so that imbalance occurs again. We think this behavior is universal and stems from the Navier-Stokes dynamics. It is also natural that the transverse structure functions are larger than those of the isotropy relations, since a relaxed state is approximately a vortical flow with the Beltrami property. The Beltrami property suppresses vortex stretching, or the nonlinearity in the Navier-Stokes equation. Further study on the decaying state may provide useful insights concerning the problem of relaxation to equilibrium and the steady solutions of the Euler equations [32–34].

This interpretation is consistent with our previous results for grid turbulence [7,8]. The sub-Gaussian PDF of the ve-

locity field in the developing state is due to the strong quasiperiodic motions, whose scale is large. When the turbulence is fully developed, motions of energy-containing eddies are random and the Fourier transforms are statistically independent of each other. Hence the velocity PDF is Gaussian. The super-Gaussian PDF in the decaying state is due to the intermittently surviving strong coherent eddies.

A comparison between Figs. 3 and 4 implies that at the smallest scales, $r \lesssim \eta$, the longitudinal structure functions always tend to be smaller than the transverse ones, which is analogous to the anisotropy at large scales in the decaying state [35]. This anisotropy at the smallest scales may be due to the existence of vortex tubes.

The Reynolds number dependence can be seen by the results for $N=256$ and 512. As expected, the fully developed state at the higher Reynolds number shows better isotropy and remains for a longer time. We have also examined the isotropy relations for the fields starting from a Gaussian random field without vortex structures. When k_0 in Eq. (6) is not so large, the field shows anisotropy as a fluctuation, which is due to the discreteness of Fourier modes. Although the fluctuation in the developing state was relatively large, the behavior in Fig. 4(a) was observed for most cases at the transition time from the developing state to the fully developed state. Both fluctuations in the fully developed and the decaying states were small, and the behaviors in Figs. 4(b) and 4(c) were commonly observed.

We now compare our results with previous work and show other possible interpretations. In Sec. III of Ref. [13], the KHK relation is examined for grid turbulence, and those results are consistent with our results in the developed state. In Ref. [30], the isotropy and the KHK relations are investigated numerically for decaying and forced turbulences. Our results agree with those for decaying turbulence. Figure 3 in Ref. [30] gives an intermediate appearance between our Figs. 4(a) and 4(b). The slow convergence for the forced turbulence reported there may be explained by the idea that a forced steady turbulence corresponds to a transition state just before the fully developed state in decaying turbulence. The forcing term in [30] induces organized vortical flow at large scales, as observed in our developing state.

The generalized KHK relations are examined experimentally in Refs. [36,12]. In the Appendix, our results for the generalized KHK relations are shown to make a detailed comparison. As discussed in the Appendix, the measured position for the grid turbulence in Ref. [36] may be slightly upstream for the test section of a fully developed state. And, in the light of our results, the channel turbulence in Ref. [12] corresponds to a developing state in our decaying turbulence. The boundary induces persistent shear and vortical flows at large scales, which resemble the flow structure behind grids.

Reconsidering the forced turbulence in Ref. [30] in view of the results in the Appendix, if the generalized KHK relations had been examined in [30], then the results would be improved, since the anisotropy is not so strong. It is an interesting problem to clarify whether embedded spherical symmetry [14–17] in turbulent flows recovers the KHK relation in such a case.

Antonia and Burattini [37] estimated Re_λ to attain the 4/5 law at a value exceeding 10^4, which is too high to use in experiments and simulations. On the other hand, it has long been known that downstream of a grid there appear three distinct flow regions. These three regions have been determined by examining statistical quantities as in Table I [7,18,19]. The KHK relation can give a good indicator to characterize and determine a test section for isotropic turbulence in a wind tunnel, in addition to the conventional ones.

Since we have confirmed that there exists an interval of the distance d where the KHK relation holds well up to extremely large scales in our experimental data, the data are appropriate to examine the decay law and the Loitsianskii constant. This is now under consideration and will be reported elsewhere. It is our intent to measure three components of the velocity and clarify the nature of the Taylor frame.

ACKNOWLEDGMENTS

We would like to acknowledge comments from an anonymous referee to improve the manuscript. We thank Professor Kida and Professor Ohkitani for comments on the draft. The numerical calculations were carried out on SX8 at YITP at Kyoto University.

APPENDIX: GENERALIZED KHK RELATION

Several generalizations of the KHK relation have been proposed to relax the assumptions in the derivation [13,38–41]. Some historical remarks are found in Ref. [42]. Comparison with the results for generalized KHK relations will help us reveal which assumption is broken in any field analyzed.

1. Generalized KHK relation in the Taylor frame

We have also examined a generalized KHK relation

$$-\frac{1}{r^2}\int_0^r \frac{\partial}{\partial t}(D_{LL}+2D_{TT})s^2 ds-(D_{LLL}+2D_{LTT}) + 2\nu\frac{\partial}{\partial r}(D_{LL}+2D_{TT})=\frac{4}{3}\epsilon r, \tag{A1}$$

which was derived by Hill [40] under the postulates of the Navier-Stokes equation, incompressibility, local homogeneity, and local isotropy. The word *local* means local with respect to r [11,40]. A direct translation of Eq. (A1) to the one in the Taylor frame may be obtained by replacing $\partial/\partial t$ with $-U\partial/\partial x$ [13]. The third component of the velocity was not measured in our experiment. Since our wind tunnel as well as the grid have comparable sizes in the spanwise and floor-normal directions, we expect the statistical quantities of the transverse velocity to be well estimated by those of v.

The results shown in Fig. 7, where each term in the LHS of Eq. (A1) is normalized by $4\epsilon r/3$, are almost the same as those in Fig. 5. Since ϵ in this case is estimated by $(\epsilon_u+\epsilon_v)/2$, which is larger than ϵ_v as known from Table I, all the graphs at large scales are shifted downward slightly. The value is still larger (smaller) than unity when the turbulence is in the developing (decaying) state. Hence we notice that

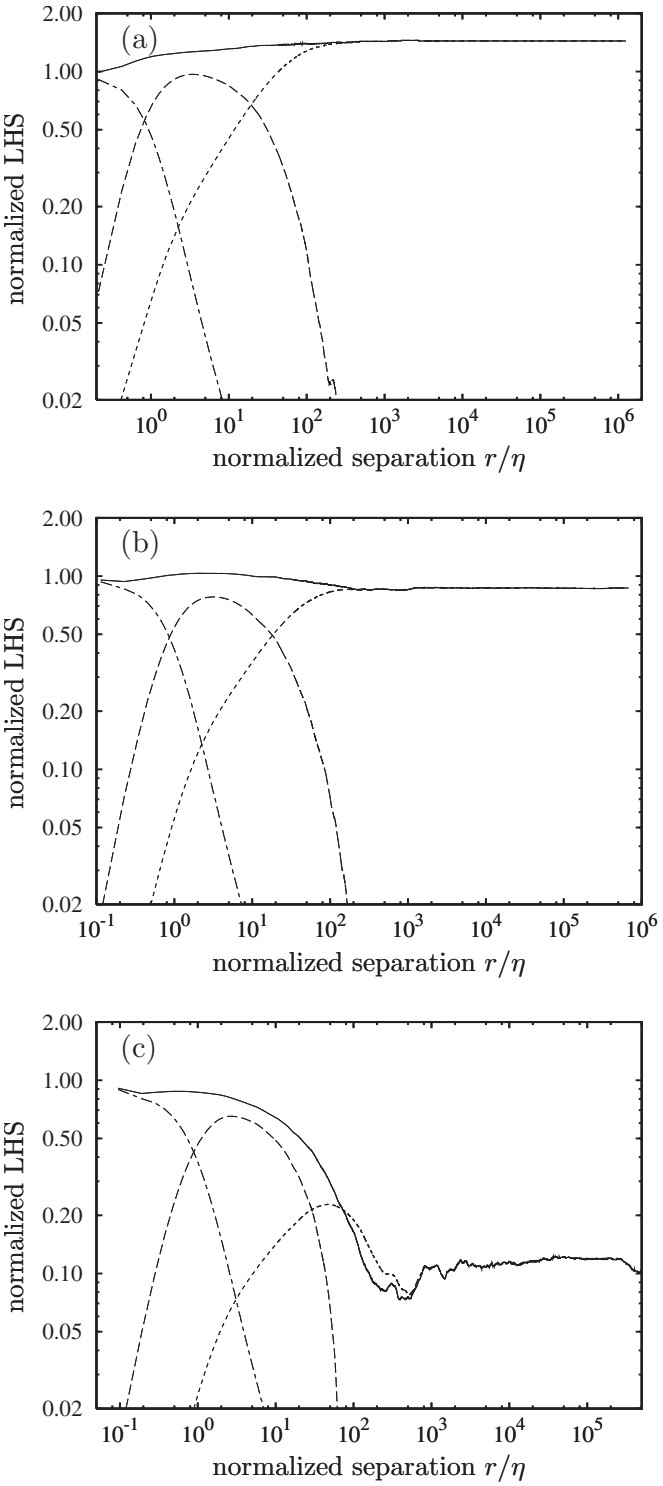

FIG. 7. Generalized KHK relation (A1) at (a) 4, (b) 10, and (c) 15 m. See also the caption of Fig. 5.

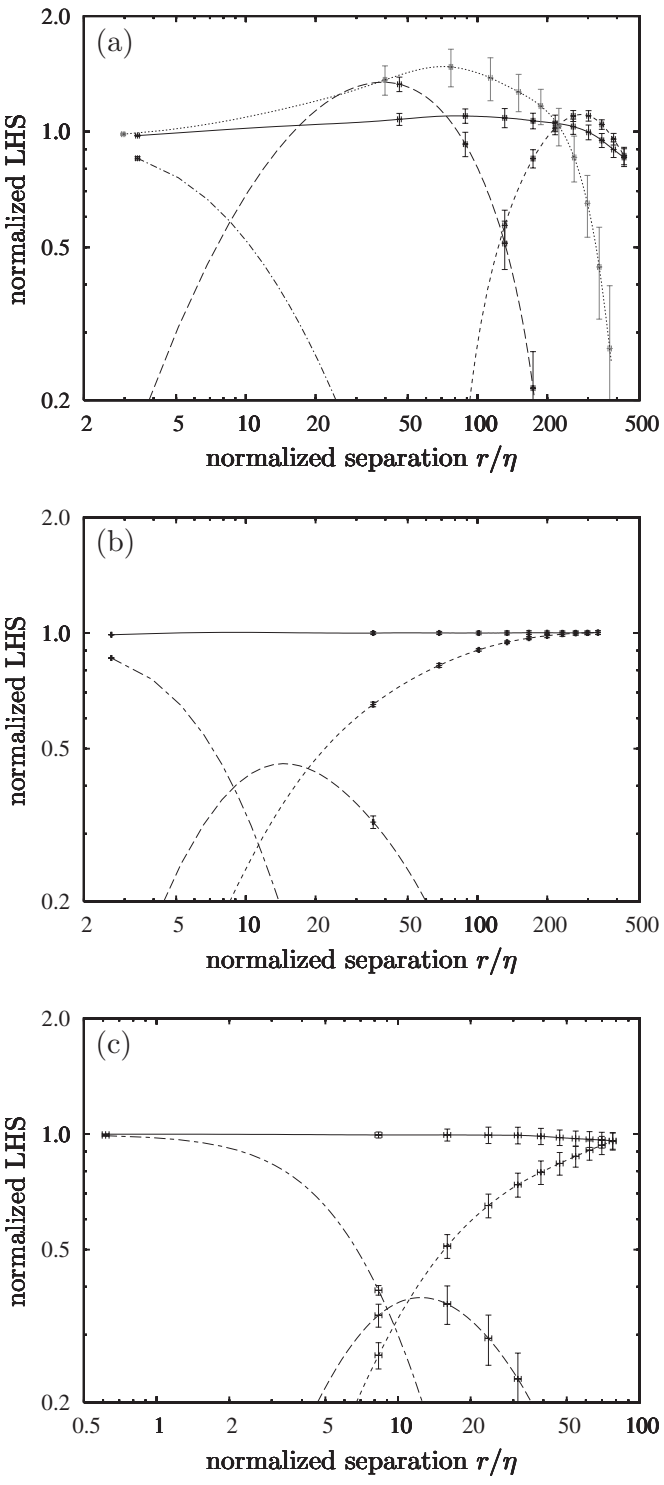

FIG. 8. Generalized KHK relation (A2) at t=(a) 0.8, (b) 2.0, and (c) 15. See also the caption of Fig. 6. The gray line in (a) is the result at t=0.6.

local isotropy as well as isotropy is broken in the field at 4 and 15 m.

Our results are seemingly different from those in Ref. [36]. The deviation from unity for the KHK relation (their Fig. 8) goes away in using a generalized KHK relation (their Fig. 9), which seems to contradict our results [Figs. 5(a) and 7(a)] at 4 m. The authors of [36] estimated ϵ by a large-scale expression $-Ud\langle q^2/2\rangle/dx$, but this is not an essential reason. This paradox will be resolved in the following section.

Figures 3 and 4 in Ref. [12] show, respectively, the result of the KHK relation and the generalized KHK relation in channel turbulence. Care should be taken in looking at these figures, since ϵ was estimated by a small-scale expression $15\nu\langle(\partial_1 u_1)^2\rangle$ in the former and by a large-scale expression

$-\partial_3\langle u_3 u_i^2\rangle$ in the latter, so that each relation must be satisfied at small (large) scales in the former (latter). Comparing the box symbols with the solid line in these figures, we recognize that both figures show a similar trend with our figures at 4 m. Channel turbulence has similar characteristics to the developing state in our decaying turbulence.

2. Generalized KHK relation in the discrete Fourier frame

Since all physical quantities can be calculated in numerical simulations, we also have examined a generalized KHK relation for $(\delta q)^2=(\delta u)^2+(\delta v)^2+(\delta w)^2$:

$$-\frac{1}{r^2}\int_0^r \frac{\partial\langle(\delta q)^2\rangle}{\partial t}s^2 ds - \langle \delta u_L(\delta q)^2\rangle + 2\nu\frac{\partial\langle(\delta q)^2\rangle}{\partial r} = \frac{4}{3}\epsilon r, \tag{A2}$$

whose expression is used to emphasize the difference from Eq. (A1). This relation is also derived under the same postulates [40].

The characteristics of the evolutions shown in Fig. 8 are almost the same as those in Fig. 6 except for the diminished deviation from unity. This diminishing means that redistribution of energy to become isotropic is active and local isotropy is almost satisfied except for the largest scales in all the fields for Fig. 8.

The gray line in Fig. 8(a) represents the sum of the normalized quantities in the LHS of Eq. (A2) at $t=0.6$. The deviation from unity is larger at earlier times, namely, if the vortex stretching is strong enough to break the local isotropy, then the generalized KHK relation as well as the KHK relation are not satisfied. The drop at the largest scales stems from the initial condition which lacks energy at these scales. We have confirmed this fact by changing the constants (k_x,k_y,k_0) in Eq. (6).

We here find a solution to the paradox raised in the previous section. Figures 6(a) and 8(a) are the same as Figs. 8 and 9 in Ref. [36]. As stated above, the field may recover the relation if the anisotropy of the field is not very strong, similar to our periodic-box turbulence at $t=0.8$. The field for Figs. 8 and 9 in [36] was not isotropic but almost satisfied local isotropy.

The authors of [36] also argued that, while large-scale anisotropy leads to an imbalance in the KHK relation, Eq. (A2) is satisfied at all scales when ϵ is measured from three components of velocity. Alternatively, it could be argued that the diminishing of the deviation from unity in our case is due not to the estimation of ϵ but to the expression of Eq. (A2), because ϵ is estimated by $2\nu\Omega$ in both Eqs. (2) and (A2), which is exact in the discrete Fourier frame.

Last, we will discuss a distinctive feature in the discrete Fourier frame. One may expect that the first term in the LHS of (A2) is equal to the RHS at the largest scales, since one assumes $\partial[(u^2+v^2+w^2)/2]/\partial t=\epsilon$. However, in the discrete Fourier frame, $(\delta q)^2$ is not always a constant at the large scales, since there usually exists a correlation at the largest scale due to its boundary condition. When the normalized unsteadiness term becomes constant, it is equal to unity as shown in Fig. 8(b). But it deviates from unity depending on the slope at the largest scales, as observed in the developing and the decaying states [see Figs. 6(a), 6(c), 8(a), and 8(c)]. If the bulk of turbulence energy is concentrated in organized vortices whose sizes are comparable with the periodic length, the constancy of the normalized unsteadiness term will be broken.

[1] T. von Karman and L. Howarth, Proc. R. Soc. London, Ser. A **164**, 192 (1938).
[2] A. N. Kolmogorov, Dokl. Akad. Nauk SSSR **32**, 16 (1941).
[3] G. K. Batchelor, Proc. Cambridge Philos. Soc. **43**, 553 (1947).
[4] L. D. Landau and E. M. Lifshitz, *Fluid Mechanics* (Pergamon, Oxford, 1959).
[5] A. N. Kolmogorov, Dokl. Akad. Nauk SSSR **30**, 301 (1941).
[6] A. N. Kolmogorov, Dokl. Akad. Nauk SSSR **31**, 538 (1941).
[7] H. Mouri, M. Takaoka, A. Hori, and Y. Kawashima, Phys. Rev. E **65**, 056304 (2002).
[8] H. Mouri, M. Takaoka, A. Hori, and Y. Kawashima, Phys. Rev. E **68**, 036311 (2003).
[9] H. Mouri, M. Takaoka, A. Hori, and Y. Kawashima, Phys. Fluids **18**, 015103 (2006).
[10] G. I. Taylor, Proc. R. Soc. London, Ser. A **151**, 421 (1935).
[11] A. S. Monin and A. M. Yaglom, *Statistical Fluid Mechanics* (MIT Press, Cambridge, MA, 1975), Vol. 2.
[12] L. Danaila, F. Anselmet, T. Zhou, and R. A. Antonia, J. Fluid Mech. **430**, 87 (2001).
[13] L. Danaila, F. Anselmet, and R. A. Antonia, Phys. Fluids **14**, 2475 (2002).
[14] Q. Nie and S. Tanveer, Proc. R. Soc. London, Ser. A **455**, 1615 (1999).
[15] I. Arad, B. Dhruva, S. Kurien, V. S. L'vov, I. Procaccia, and K. R. Sreenivasan, Phys. Rev. Lett. **81**, 5330 (1998).
[16] I. Arad, L. Biferale, I. Mazzitelli, and I. Procaccia, Phys. Rev. Lett. **82**, 5040 (1999).
[17] M. A. Taylor, S. Kurien, and G. L. Eyink, Phys. Rev. E **68**, 026310 (2003).
[18] M. S. Mohamed and J. C. LaRuc, J. Fluid Mech. **219**, 195 (1990).
[19] R. Tresso and D. R. Munoz, J. Fluids Eng. **122**, 51 (2000).
[20] We define both the Reynolds number and the Taylor microscale in terms of v, which is free from contamination by the w component. See also N. K. Tutu and R. Cheveray, J. Fluid Mech. **71**, 785 (1975).
[21] In isotropic turbulence, the longitudinal integral length $L_u=\int\langle u(x+\delta x)u(x)\rangle/\langle u(x)^2\rangle d\delta x$ is just $2L_v$. The calculated L_u, omitted from Table I, seems to be larger than the expected value due to the slow decay of the longitudinal-velocity correlation.
[22] M. Takaoka, J. Phys. Soc. Jpn. **66**, 2008 (1997).
[23] L. G. Loitsianskii, Cent. Aero. Hydro Inst., Moscow, Rep. **440**, 3 (translation in NACA TM. 1079) (1939).

[24] For turbulence starting from $E(k,0) \sim k^s$ $(s \geq 4)$ at small k, the energy spectrum grows as k^4 at small k, if Loitsianskii's integral is invariant.
[25] S. Kida and Y. Murakami, Phys. Fluids **7**, 2030 (1987).
[26] M. Lesieur, O. Métais, and P. Comte, *Large-Eddy Simulations of Turbulence* (Cambridge University Press, Cambridge, U.K., 2005).
[27] G. R. Ruetsch and M. R. Maxey, Phys. Fluids A **4**, 2747 (1992).
[28] J. Jimenez, A. A. Wray, P. G. Saffman, and R. S. Rogallo, J. Fluid Mech. **255**, 65 (1993).
[29] T. von Karman, J. Aeronaut. Sci. **4**, 131 (1937).
[30] D. Fukayama, T. Oyamada, T. Nakano, T. Gotoh, and K. Yamamoto, J. Phys. Soc. Jpn. **69**, 701 (2000).
[31] L is not equal to the original value $\int \langle u(x)u(x+r)\rangle / \langle u(x)^2\rangle dr$, which gives the periodic length.
[32] H. Moffatt, J. Fluid Mech. **159**, 359 (1985).
[33] R. Kraichnan and R. Panda, Phys. Fluids **31**, 2395 (1988).
[34] G. C. G. K. Vallis and W. Young, J. Fluid Mech. **207**, 133 (1989).
[35] The dashed lines at scales smaller than the integral length are always below the solid lines in Fig. 3. This is partly due to the fact that the u component is more susceptible to spiky electric noise than the v component.
[36] P. Lavoie, P. Burattini, L. Djenidi, and R. Antonia, Exp. Fluids **39**, 865 (2005).
[37] R. A. Antonia and P. Burattini, J. Fluid Mech. **550**, 175 (2006).
[38] A. S. Monin, Dokl. Akad. Nauk SSSR **125**, 515 (1959).
[39] U. Frisch, *Turbulence* (Cambridge University Press, Cambridge, U.K., 1995).
[40] R. J. Hill, J. Fluid Mech. **353**, 67 (1997).
[41] S. Kurien, Physica D **175**, 167 (2003).
[42] G. L. Eyink and R. Sreenivasan, Rev. Mod. Phys. **78**, 87 (2006).